

Balancing Act: Trading Off Doppler Odometry and Map Registration for Efficient Lidar Localization

Katya M. Papais¹, Daniil Lisus¹, David J. Yoon¹, Andrew Lambert²,
Keith Y.K. Leung², and Timothy D. Barfoot¹

Abstract—Most autonomous vehicles rely on accurate and efficient localization, which is achieved by comparing live sensor data to a preexisting map, to navigate their environment. Balancing the accuracy of localization with computational efficiency remains a significant challenge, as high-accuracy methods often come with higher computational costs. In this paper, we present two ways of improving lidar localization efficiency and study their impact on performance. First, we integrate a lightweight Doppler-based odometry method into a topometric localization pipeline and compare its performance against an iterative closest point (ICP)-based method. We highlight the trade-offs between these approaches: the Doppler estimator offers faster, lightweight updates, while ICP provides higher accuracy at the cost of increased computational load. Second, by controlling the frequency of localization updates and leveraging odometry estimates between them, we demonstrate that accurate localization can be maintained while optimizing for computational efficiency using either odometry method. Our experimental results show that localizing every 10 lidar frames strikes a favourable balance, achieving a localization accuracy below 0.05 m in translation and below 0.1° in orientation while reducing computational effort by over 30% in an ICP-based pipeline. We quantify the trade-off of accuracy to computational effort using over 100 km of real-world driving data in different on-road environments.

I. INTRODUCTION

A critical part of autonomous vehicle (AV) navigation is the ability to localize the vehicle in a known map of the environment. This task, called localization, is crucial for down-stream AV objectives such as trajectory planning and optimization, obstacle tracking and avoidance, and smooth vehicle handling.

A map-based localization pipeline will conventionally contain two parts: a frame-to-frame, relative-motion odometry estimator, and a frame-to-map localization estimator [1], [2]. A common technique employed in both estimators when using a lidar sensor is the iterative closest point (ICP) algorithm, which iteratively aligns two pointclouds [3], [4]. The odometry estimator matches lidar pointclouds between consecutive frames, while the localization estimator matches the live lidar pointcloud to a pointcloud map, typically constructed using lidar data from a previous traversal. To get state-of-the-art (SOTA) localization performance, a large

This work was supported by the OGS Program provided by the Province of Ontario, and the NSERC CGS D scholarship.

¹University of Toronto Institute for Aerospace Studies, 4925 Dufferin Street, Toronto, Ontario, Canada. {katya.papais, daniil.lisus, david.yoon}@robotics.utoronto.ca, tim.barfoot@utoronto.ca

²Trimble, Richmond Hill, Ontario, Canada. {andrew_lambert, keith_leung}@trimble.com

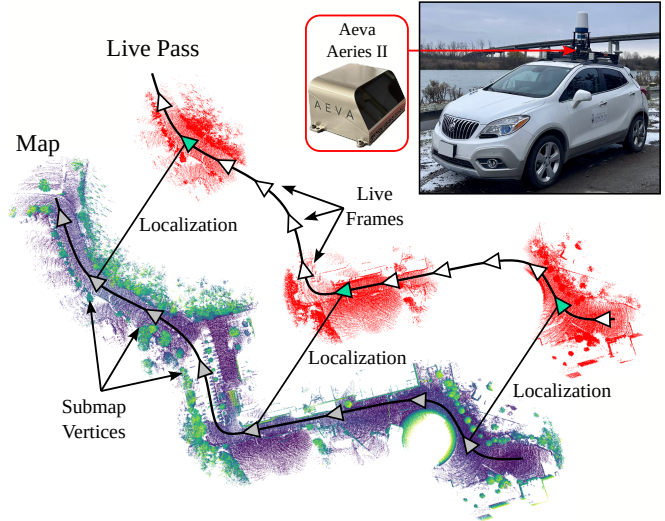


Fig. 1. We explore the trade-off between computational efficiency and localization accuracy with infrequent map matching, analyzing how dead-reckoning between these localization attempts impacts overall performance. Top right is our data collection platform, Boreas, equipped with an Aeva Aeries II FMCW lidar sensor.

number of lidar points and many ICP iterations are needed for both estimators; this process can quickly become computationally expensive. Thus, there is an inherent trade-off between accuracy and computational efficiency.

Our previous work began quantifying this trade-off for stand-alone odometry estimators through the use of frequency-modulated continuous-wave (FMCW) lidar sensors, which return per-point radial velocity data via the Doppler effect [5], [6]. We showed that using radial velocity measurements in a correspondence-free ‘Doppler odometry’ estimator allowed for estimation to occur significantly faster than in an ICP-based SOTA odometry estimator, albeit at the cost of accuracy [6].

This paper extends the study of computational efficiency in lidar-based navigation to localization. First, we incorporate the lower-quality but faster odometry method from [6] into a localization pipeline. Second, we compare the odometry methods presented in [1] and [6] to investigate how the final localization result is affected when odometry is used to dead-reckon for progressively longer intervals between map-matching updates. This creates a wide range of possible runtimes and accuracies: from infrequent localization calls using Doppler odometry, to running localization at every frame using ICP-based odometry. Achieving the right bal-

ance between these methods requires careful consideration of how frequently to localize against a map. Localizing too frequently with ICP increases computational demand, whereas relying too heavily on Doppler odometry can reduce localization accuracy over time.

Our contributions are summarized as follows:

- We present the novel integration of a lightweight Doppler odometry method within a localization pipeline as an efficient alternative to an ICP-based method.
- We explore the trade-off between computational effort and localization performance by varying the frequency of localization updates in two odometry algorithms.

The rest of this paper is structured as follows. Section II presents relevant prior work. Section III discusses the details of the implemented pipelines. Section IV shows and discusses the experimental results. Section V highlights the main conclusions.

II. RELATED WORK

A. ICP-based Lidar Odometry

ICP-based lidar odometry estimates the relative transformation between two pointclouds by iteratively associating points using nearest-neighbour search [3], [4]. Since ICP-based methods can become computationally expensive when using dense lidar pointclouds, many SOTA methods implement optimizations, such as voxel downsampling, to achieve real-time performance [7]–[9].

A limitation to conventional ICP-based methods is the discrete-frame assumption, which can introduce misalignment when motion occurs throughout a frame. To address this, continuous-time ICP methods estimate the trajectory as a smooth function of time, allowing pose estimates to vary throughout each frame [5], [8], [9]. The ICP-based odometry method used in this work is most similar to the CT-ICP method presented by Dellenbach *et al.* [8], leveraging a continuous-time representation to improve robustness.

Another challenge for conventional ICP methods is geometrically degenerate environments. This challenge is typically overcome through the integration of additional sensors, such as inertial measurement units (IMU) [9]–[14]. Zhao *et al.* [11] follow a loosely coupled approach, using a dynamic octree to achieve real-time performance. Shan *et al.* [12] instead follow a tightly coupled approach, using IMU preintegration to deskew pointclouds. To achieve real-time performance, their system uses a sliding window-based approach for local scan-matching. In this work, we include gyroscope measurements directly in our ICP-based odometry optimization problem, and undistort pointclouds using the posterior of our estimated trajectory, similar to [14].

B. ICP-based Lidar Localization

Global Navigation Satellite System (GNSS) sensors are commonly used in combination with lidar sensors to perform vehicle localization. For example, Yoneda *et al.* [15] use ICP to align live lidar pointclouds to a geo-referenced map to study the use of Mobile Mapping Systems in AV navigation. However, GNSS positional accuracy degrades in complex or

rapidly changing environments, making it unreliable in urban canyons or tunnels. In such cases, topometric localization offers a solution by matching onboard sensor data to a prebuilt map of the environment [1], [16]–[18]. This paper follows the work of Burnett *et al.* [1], performing ICP-based localization within a pose-graph-based topometric map. This approach allows to incorporate measurements as they arrive. While our work makes use of a topometric localization pipeline to study the trade-off between accuracy and computational efficiency, the idea of restricting the frequency of localization updates can be applied to other localization pipelines.

C. Lidar Navigation Efficiency

Several papers discuss and attempt to improve the trade-off between computational effort and performance in lidar-based localization and other lidar-based navigation tasks [13], [19], [20]. Niedzwiedzki *et al.* [19] present a real-time lidar localization algorithm for GPS-denied environments. The algorithm applies an extended Kalman filter to each lidar point and localizes a robot relative to a triangular mesh reference map. This approach creates a compact map representation, thus reducing computational cost, without a significant reduction in accuracy. The work by Zhang *et al.* [13] is most similar to ours in that fast, low-fidelity odometry estimates at 10 Hz are refined by slower, high-fidelity localization updates at 1 Hz. While this approach is common in simultaneous localization and mapping (SLAM) systems, where continuous map-building and updating are essential to achieve real-time [13], [20], our work differs in that we use a prebuilt reference map and analyze the trade-offs associated with SOTA localization. To the best of our knowledge, none have studied the impact of infrequent map matches for optimizing computational efficiency and accuracy in a localization pipeline.

D. FMCW Sensors

1) *Lidar*: Recent work has introduced the use of FMCW lidar sensors, which return per-point radial velocity data using the Doppler effect in addition to 3D point locations [5], [6], [21], [22]. Unlike traditional time-of-flight lidar, FMCW lidar sensors also offer enhanced range resolution, detection sensitivity, and resistance to interference [23]. By incorporating the velocity measurements into ICP-based methods, estimation robustness has been shown to improve in geometrically degenerate environments [5], [24]. Hexsel *et al.* [24] first showed that Doppler velocity measurements can be used for motion estimation methods using the Doppler-ICP algorithm. Wu *et al.* [5] built upon this by incorporating a continuous-time estimator and eliminating the need for external motion compensation when preprocessing data.

Yoon *et al.* [6] showed that data association between pointclouds can be eliminated entirely with their lightweight, correspondence-free odometry solution. The quantitative results of their proposed method show that it is significantly faster than state-of-the-art ICP-based odometry while being reasonably accurate. Our work introduces the use of this odometry algorithm within a localization pipeline.

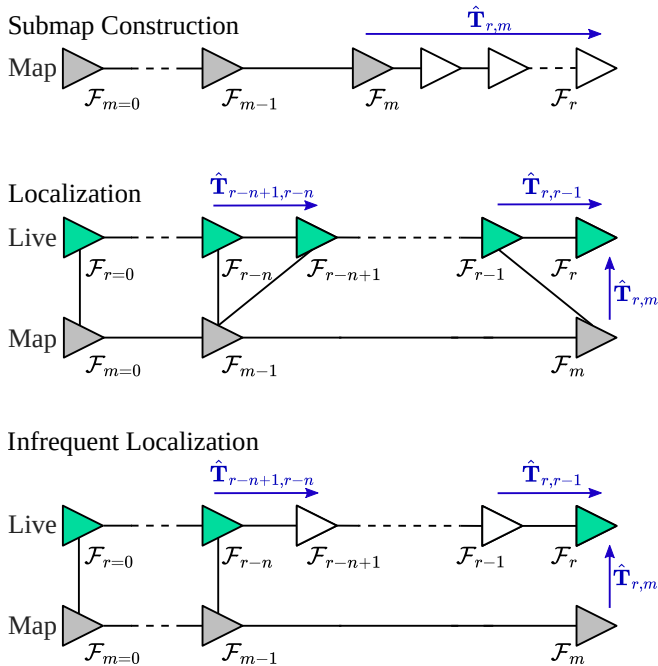


Fig. 2. The structure of the pose graph during submap construction and localization, comparing the localization pipeline from [1] to the modified pipeline used in this work.

2) *Radar*: Similar work for motion estimation has been done using FMCW radar technology [25]–[31]. Kramer *et al.* [27] incorporate IMU data with the Doppler measurements to form a lightweight velocity estimator on a small experimental sensor rig. Kubelka *et al.* [29] and Lisus *et al.* [31] show that incorporating radar Doppler measurements with IMU data can yield comparable or superior results compared to ICP-based radar methods. In this work, we use FMCW lidar, but the presented approach can be extended to FMCW radar.

III. METHODOLOGY

A. Problem Formulation

We use the teach and repeat framework as our localization pipeline [1], [17], [32], [33]. During the initial ‘teach’ phase, the vehicle collects sensor data along a route, which is used to construct local submaps stored as vertices in a pose graph. These vertices are connected by edges representing relative pose estimates, which are based on odometry. Fig. 1 and 2 show odometry estimates and submap vertices as white and grey nodes, respectively.

During the ‘repeat’ phase, the vehicle follows the same route, again using odometry estimates to build a new branch of the pose graph while simultaneously localizing against the previously recorded submaps. This localization step corrects for odometric drift without relying on global positioning. Odometry estimates that are localized against a submap are coloured green in Fig. 1 and 2.

Fig. 2 shows the original pipeline used in Burnett *et al.* [1] in the middle and our modified pipeline on the bottom. We use the following notation:

- r denotes the current frame being estimated,

- m denotes the submap vertex from the teach pass,
- n denotes the number of frames between successive attempts to localize,
- $\hat{\mathbf{T}}_{r,r-1}$ denotes the latest odometry estimate from the previous frame, \mathcal{F}_{r-1} , to the current frame \mathcal{F}_r ,
- $\hat{\mathbf{T}}_{r,m}$ denotes the localization estimate from the submap vertex, \mathcal{F}_m , to the current frame, \mathcal{F}_r .

The goal of odometry is to estimate $\hat{\mathbf{T}}_{r,r-1}$, the transformation from the previous frame \mathcal{F}_{r-1} to the current frame \mathcal{F}_r . The goal of localization is to estimate $\hat{\mathbf{T}}_{r,m}$, the transformation from the closest submap in the reference map \mathcal{F}_m to the current frame \mathcal{F}_r .

In [1], localization is attempted at every frame, where $n = 1$ (see Fig. 2, middle). In this work, we progressively increase n to study the resulting effect on computational efficiency and localization accuracy (see Fig. 2, bottom).

The following sections describe the two odometry methods and the localization procedure considered in this paper.

B. Doppler Odometry

We use the Doppler-enabled odometry methodology as presented by Yoon *et al.* [6]. We provide a summary here and refer the reader to [6] for further details.

1) *Raw Data Preprocessing*: Yoon *et al.* [6] downsample the measurements uniformly in azimuth-elevation space and apply a measurement bias correction that is mainly dependent on the range of each measurement. This correction is trained offline as a linear regression model. Doppler measurement outliers, which can be caused by moving objects or reflections in the scene, are rejected using random sample and consensus (RANSAC) [34]. In this work, we add an additional outlier rejection threshold of 3 m/s on the change in forward velocity between frames to filter out instances where RANSAC incorrectly latches onto dynamic objects due to a shortage of static points in the scene. This threshold ensures that the solutions do not greatly vary between frames, as done in [31], [35].

2) *Estimation*: The task is formulated as an exactly sparse Gaussian process (GP) regression problem, based on the work by Barfoot *et al.* [36], seeking to solve for the continuous-time 6-DOF vehicle velocity, $\varpi(t)$. This method leverages the per-point relative radial velocity measurements provided by the FMCW lidar sensor, gyroscope measurements, and a motion prior. The motion prior is modelled as white-noise-on-acceleration (WNOA),

$$\dot{\varpi}(t) = \mathbf{w}(t), \quad \mathbf{w}(t) \sim \mathcal{GP}(\mathbf{0}, \mathbf{Q}_c \delta(t - t')), \quad (1)$$

where $\varpi(t)$ is the estimated velocity, $\mathbf{w}(t)$ is a zero-mean GP with a power spectral density matrix \mathbf{Q}_c , and $\delta(\cdot)$ is the Dirac delta function. The motion prior error term is

$$\mathbf{e}_{\text{wnoa}}^r = \varpi_r - \varpi_{r-1}, \quad (2)$$

where ϖ_r are the discrete velocity states. The corresponding motion prior factor is

$$\phi_{\text{wnoa}}^r = \frac{1}{2} \mathbf{e}_{\text{wnoa}}^r T \mathbf{Q}_r^{-1} \mathbf{e}_{\text{wnoa}}^r, \quad (3)$$

where $\mathbf{Q}_r = (t_r - t_{r-1})\mathbf{Q}_c$ is constant because the discrete states, ϖ_r , are uniformly spaced in time [37].

Yoon *et al.* [6] also incorporate vehicle kinematics by penalizing velocities in the lateral, vertical, roll, and pitch dimensions. The vehicle kinematics error is defined as

$$\mathbf{e}_{\text{kin}}^r = \mathbf{H}\varpi_r, \quad (4)$$

where \mathbf{H} is a constant matrix that extracts the desired dimensions. The corresponding factor is

$$\phi_{\text{kin}}^r = \frac{1}{2}\mathbf{e}_{\text{kin}}^r{}^T \mathbf{Q}_z^{-1} \mathbf{e}_{\text{kin}}^r, \quad (5)$$

where \mathbf{Q}_z is the associated covariance.

The Doppler measurement model and the gyroscope measurement model are both linear with respect to the vehicle velocity, making this approach particularly efficient. The Doppler measurement error model is

$$e_{\text{dop}}^i = y_{\text{dop}}^i - \frac{1}{\|\mathbf{q}_s^i\|} \begin{bmatrix} \mathbf{q}_s^i{}^T & \mathbf{0} \end{bmatrix} \mathcal{T}_{s,v} \varpi(t_i) - h(\psi^i), \quad (6)$$

where y_{dop}^i is the i^{th} Doppler measurement, $\mathbf{q}_s^i \in \mathbb{R}^3$ are the corresponding point coordinates in the sensor frame, $\mathcal{T}_{s,v} \in \text{Ad}(SE(3))$ is the known extrinsic adjoint transformation between the sensor and vehicle frames, and $\varpi(t_i) \in \mathbb{R}^6$ is the continuous-time vehicle velocity at the measurement time i . Since this error model is scalar, the corresponding measurement factor is

$$\phi_{\text{dop}}^i = \frac{1}{2}(e_{\text{dop}}^i)^2 R_{\text{dop}}^{-1}, \quad (7)$$

where R_{dop} is the variance of the Doppler measurements.

The gyroscope error model is

$$\mathbf{e}_{\text{gyro}}^j = \mathbf{y}_{\text{gyro}}^j - \mathbf{C}_{s,v} \mathbf{D} \varpi(t_j), \quad (8)$$

where $\mathbf{y}_{\text{gyro}}^j \in \mathbb{R}^3$ is the j^{th} angular velocity measurement in the sensor frame, $\mathbf{C}_{s,v} \in SO(3)$ is the known extrinsic rotation between the vehicle and sensor frames, \mathbf{D} is a constant 3×6 selection matrix removing the translational components of the body velocity, and $\varpi(t_j)$ is the continuous-time vehicle velocity at the measurement time j [6]. The corresponding measurement factor is

$$\phi_{\text{gyro}}^j = \frac{1}{2}\mathbf{e}_{\text{gyro}}^j{}^T \mathbf{R}_{\text{gyro}}^{-1} \mathbf{e}_{\text{gyro}}^j, \quad (9)$$

where \mathbf{R}_{gyro} is the gyroscope covariance [6].

The objective function we seek to optimize is a sum over all of these factors:

$$J_{\text{dop}} = \sum_r (\phi_{\text{wnoa}}^r + \phi_{\text{kin}}^r) + \sum_i \phi_{\text{dop}}^i + \sum_j \phi_{\text{gyro}}^j. \quad (10)$$

Since all of the error models are linear in velocity, solving the resulting linear system is computationally efficient [6].

Once the vehicle velocity is estimated, we approximate the relative pose by numerically integrating the velocity over time. This is done by sampling $\varpi(t)$ at small time intervals, Δt , and constructing a sequence of $SE(3)$ transformations

that represent the motion over the lidar frame. The transformation between two consecutive frames is computed as

$$\hat{\mathbf{T}}_{r-1,r} \approx \prod_{i=1}^S \exp(\Delta t \varpi(t_{r-1} + i\Delta t)), \quad (11)$$

where S is the number of interpolation steps, $\exp(\cdot)$ is the exponential map, $(\cdot)^\wedge$ transforms an element of \mathbb{R}^6 into a member of Lie algebra $\mathfrak{se}(3)$ [38], and $\varpi(t)$ is the vehicle velocity interpolated between the frame boundary velocities ϖ_{r-1} and ϖ_r .

C. ICP Odometry Baseline

We use the estimation methodology as presented by Burnett *et al.* [1]. We provide a summary here and refer the reader to [1] for further detail.

1) *Raw Data Preprocessing*: Following the method presented in [1], each lidar scan undergoes voxel downsampling, where only the point closest to the centre of each voxel is retained. Plane features are then extracted from the scene using principle component analysis (PCA), with each point assigned a feature score based on its eigenvalues. Points with a feature score greater than 0.95 are kept, and each point is then associated with the eigenvector corresponding to the smallest eigenvalue from PCA, which serves as its normal.

2) *Estimation*: The continuous-time ICP approach from [1] extends traditional ICP by representing the trajectory as an exactly sparse GP [37]. The trajectory is modelled as a pair consisting of the vehicle's pose and 6-DOF velocity, $\mathbf{x}(t) = \{\mathbf{T}(t), \varpi(t)\}$, and the goal is to minimize a nonlinear optimization problem to estimate the state. We use the same WNOA motion prior as in (1), with the addition of a kinematic model that relates the robot's body-centric velocity to its pose. The error term associated with the constant velocity prior, $\mathbf{e}_{\text{prior}}$, follows the definition in [37]. The corresponding motion prior factor is

$$\phi_{\text{prior}} = \frac{1}{2}\mathbf{e}_{\text{prior}}{}^T \mathbf{Q}_{\text{prior}}^{-1} \mathbf{e}_{\text{prior}}, \quad (12)$$

where $\mathbf{Q}_{\text{prior}}$ is the associated covariance.

Each point in the scan is motion-compensated based on the current trajectory estimate associated with its nearest neighbour in the submap. The measurement error model is

$$\mathbf{e}_{\text{icp}}^i = \mathbf{D} (\mathbf{p}_m^i - \mathbf{T}_{r,m}^{-1}(t_i) \mathbf{T}_{r,s} \mathbf{q}_i), \quad (13)$$

where \mathbf{q}_i is a homogeneous point at timestamp t_i from the r^{th} lidar scan, \mathbf{p}_m^i is a homogeneous point from the m^{th} submap associated to \mathbf{q}_i , $\mathbf{T}_{r,s}$ is the extrinsic transformation between the sensor and vehicle frames, $\mathbf{T}_{r,m}(t_i)$ is the pose from the trajectory queried at timestamp t_i , and \mathbf{D} is a constant selection matrix that removes the fourth element. The measurement factor for the estimation problem is

$$\phi_{\text{icp}}^i = \frac{1}{2}\mathbf{e}_{\text{icp}}^i{}^T \mathbf{R}_i^{-1} \mathbf{e}_{\text{icp}}^i, \quad (14)$$

where \mathbf{R}_i is the lidar measurement covariance.

In this work, gyroscope data is also incorporated into the ICP-based estimation to improve accuracy and make

it comparable to the Doppler-based estimator. We use the same error term as in (8) along with the corresponding measurement factor as in (9).

The nonlinear cost function,

$$J_{\text{icp}} = \phi_{\text{prior}} + \sum_i \phi_{\text{icp}}^i + \sum_j \phi_{\text{gyro}}^j, \quad (15)$$

is iteratively optimized for the trajectory $\mathbf{x}(t)$ using Gauss-Newton optimization followed by nearest-neighbours data association after each iteration. The pose and velocity are updated on each iteration until the convergence criteria are met or until we reach the maximum iteration limit.

D. Mapping

All reference maps are constructed offline using ICP odometry (Section III-C) following the method presented in [1]. Mapping is achieved by incrementally building a series of local submaps that represent the vehicle’s environment. Using the odometry estimates, the system continuously monitors the vehicle’s motion, estimating the transformation between the latest submap, \mathcal{F}_m , and the current live lidar scan, \mathcal{F}_r (top of Fig. 2). When the relative motion exceeds a predefined translation or rotation threshold, a new submap vertex \mathcal{F}_{m+1} is added. The submap at each new vertex is built by accumulating pointclouds from the last three frames.

E. Localization

To ensure consistency during localization, both pipelines preprocess the pointcloud using the same method, as presented in Section III-C.1. The pointcloud is then undistorted using the respective odometry estimate. This ensures that the same filtered pointcloud is used for localization, with the only differences being the odometry prior. Further computational savings are achieved with the Doppler estimator, which does not rely on previously stored pointclouds for odometry. Instead, the preprocessed pointcloud is only stored if a localization attempt is flagged for that frame.

We use the localization methodology from [1], summarized here for completeness. During the repeat pass, the localization module relies on ICP to align the current motion-compensated lidar frame, \mathcal{F}_r , to the submap associated with the nearest vertex frame, \mathcal{F}_m , from the teach pass sequence. The nearest vertex is determined using the latest odometry estimate by traversing the edges within the pose graph to find the spatially closest candidate. The prior, $\tilde{\mathbf{T}}_{r,m}$, is constructed using a previous map match and is used to form a prior error term

$$\mathbf{e}_{\text{prior}} = \ln(\tilde{\mathbf{T}}_{r,m} \mathbf{T}_{r,m}^{-1})^\vee, \quad (16)$$

where $\mathbf{T}_{r,m}$ is the transform we seek to estimate, and $(\cdot)^\vee$ is the $SE(3)$ ‘vee’ operator [38]. The measurement error is

$$\mathbf{e}_{\text{loc}}^i = \mathbf{D}(\mathbf{p}_m^i - \mathbf{T}_{r,m}^{-1} \mathbf{T}_{r,s} \mathbf{q}_i), \quad (17)$$

where \mathbf{q}_i is a homogeneous point from the current motion-compensated pointcloud, \mathbf{p}_m^i is a homogeneous point from the m^{th} submap associated to \mathbf{q}_i , and $\mathbf{D}, \mathbf{T}_{r,s}$ are as defined in Section III-C.

The nonlinear cost function we seek to optimize is

$$J_{\text{loc}} = \frac{1}{2} \mathbf{e}_{\text{prior}}^T \mathbf{Q}_{\text{prior}}^{-1} \mathbf{e}_{\text{prior}} + \sum_i \frac{1}{2} \mathbf{e}_{\text{loc}}^i{}^T \mathbf{R}_i^{-1} \mathbf{e}_{\text{loc}}^i, \quad (18)$$

where $\mathbf{Q}_{\text{prior}}$ and \mathbf{R}_i are the covariance matrices associated with the prior and measurement error terms, respectively.

1) *Localize every frame, $n = 1$* : When localizing every frame (see Fig. 2, middle), the initial pose estimate alignment, $\tilde{\mathbf{T}}_{r,m}$, is computed by compounding the transformations between frames in the pose graph:

$$\tilde{\mathbf{T}}_{r,m} = \mathbf{T}_{r,r-1} \mathbf{T}_{r-1,m-1} \mathbf{T}_{m-1,m}. \quad (19)$$

2) *Localize every n frames*: Instead of localizing after each frame, we restrict localization to be triggered after a set number of frames, denoted by n (see Fig. 2, bottom). Between localization calls, we rely on the odometry estimates and dead-reckon for n frames. Once localization is triggered, our prior is computed by compounding the odometry estimates since the last successful localization:

$$\tilde{\mathbf{T}}_{r,m} = \mathbf{T}_{r,r-1} \mathbf{T}_{r-1,r-2} \cdots \mathbf{T}_{r-n,m-1} \mathbf{T}_{m-1,m}. \quad (20)$$

This process reduces computational overhead in the AV navigational pipeline by reducing the number of costly ICP-based map alignment calls.

IV. EXPERIMENTS

A. Data

We collected data using the Boreas vehicle near the University of Toronto Institute for Aerospace Studies [39]. Lidar data was collected using an Aeva Aeries II FMCW lidar sensor, which has a 120° horizontal field of view, a 30° vertical field of view, a maximum operating range of 500 m, and operates at 10 Hz. The lidar is equipped with an IMU, from which we use gyroscope measurements. Groundtruth was generated from GNSS, a stand-alone IMU, and wheel encoder data using Applanix’s RTX POSpac software.

We collected five sequences for three different routes totalling approximately 110 km. The ‘Glen Shields’ route, introduced in [39], is a suburban route with many static features; the ‘Commercial’ route passes through slower urban areas with clear geometric landmarks; and the ‘Highway 7’ route, introduced in [31], has a higher speed limit and is primarily on a highway with fewer static features. For each route, two holdout sequences were used to tune covariances and gyroscope biases, one sequence was used to create the reference map, and the two remaining sequences were used to generate the experimental results. The tuning process was performed on all the holdout sequences collectively to prevent overfitting to a specific route. No GPS or IMU data was used to construct the map; gyroscope data is exclusively used during the repeat pass to aid in estimation.

B. Results

1) *Evaluation Metrics*: Localization performance is quantified using the root mean squared error (RMSE) across repeat sequences for each route. The real-time ratio is defined

TABLE I

ICP-BASED ESTIMATOR: METRIC LOCALIZATION RMSE RESULTS AND AVERAGE RUNTIME PER LIDAR FRAME FOR $n = 1, 10, 150$. RMSE VALUES ARE AVERAGED ACROSS LOCALIZATION RUNS PER ROUTE.

Route	Interval (n)	Runtime [ms]	Position RMSE [m]			Orientation RMSE [°]		
			lateral	longitudinal	vertical	roll	pitch	heading
Glen Shields	1	125	0.031	0.028	0.046	0.048	0.050	0.042
	10	86	0.040	0.031	0.047	0.065	0.075	0.056
	150	80	0.136	0.074	0.072	0.088	0.115	0.198
Commercial	1	102	0.030	0.027	0.034	0.060	0.061	0.050
	10	71	0.039	0.033	0.037	0.081	0.097	0.062
	150	67	0.099	0.090	0.066	0.104	0.131	0.160
Highway 7	1	118	0.043	0.040	0.027	0.052	0.051	0.053
	10	80	0.051	0.048	0.030	0.065	0.073	0.063
	150	76	0.212	0.126	0.136	0.115	0.118	0.170

TABLE II

DOPPLER ESTIMATOR: METRIC LOCALIZATION RMSE RESULTS AND AVERAGE RUNTIME PER LIDAR FRAME FOR $n = 1, 10, 50$. RMSE VALUES ARE AVERAGED ACROSS LOCALIZATION RUNS PER ROUTE.

Route	Interval (n)	Runtime [ms]	Position RMSE [m]			Orientation RMSE [°]		
			lateral	longitudinal	vertical	roll	pitch	heading
Glen Shields	1	92	0.033	0.030	0.047	0.071	0.057	0.056
	10	17	0.047	0.045	0.058	0.144	0.131	0.151
	50	10	0.212	0.203	0.180	0.253	0.227	0.613
Commercial	1	80	0.032	0.028	0.035	0.079	0.068	0.059
	10	15	0.038	0.039	0.036	0.160	0.172	0.133
	50	9	0.149	0.127	0.104	0.249	0.258	0.436
Highway 7	1	86	0.046	0.042	0.029	0.070	0.056	0.071
	10	15	0.054	0.061	0.039	0.119	0.116	0.148
	50	8	0.210	0.211	0.141	0.194	0.202	0.571

as the ratio between runtime of the localization pipeline and the collection time of the sequence. A compute ratio of 1 indicates real-time performance. We generated all timing using a Lenovo ThinkPad P16 Gen 2 laptop with an Intel(R) Core(TM) i7-13850HX CPU and 64GB of memory. A GPU was not used. The Doppler-based pipeline is run on a single thread, while the ICP-based pipeline is run using 10 threads.

We use Pareto curves as a graphical representation of the trade-off between two competing objectives; in our case, localization accuracy and computational effort. Fig. 3 shows the performance of our pipelines across varying configurations, showing how accuracy and computational cost change relative to each other as the localization interval increases. The ‘knee point’ on the curve corresponds to the most cost-effective trade-off between computation time and accuracy. This knee point is identified by creating a rectangle between each point on the curve to the origin, with the optimal solution corresponding to the rectangle with minimal area.

Tables I and II present results for the Doppler and ICP-based pipelines at three key configurations: the most accurate, the knee point, and the fastest. For each configuration, we report the translational and rotational RMSE values, and the average runtime per frame. Per-frame runtimes below 100 ms are considered real-time for our 10 Hz lidar.

2) *Estimator Analysis*: The ICP-based estimator reaches its knee point at $n = 10$, optimally balancing accuracy and compute. Since the lidar operates at 10 Hz, this corresponds to localizing once per second. Although the estimator maintains reasonable accuracy beyond the knee point, reducing the localization frequency beyond it yields diminishing computational savings as the pipeline’s runtime becomes bottlenecked by the odometry method. ICP’s robustness against drift allows it to maintain accuracy with fewer corrections, extending its useful range to higher intervals than the Doppler estimator. However, this method struggles to achieve real-time performance when using smaller intervals. Using our approach, the ICP-based method achieves real-time performance when $n \geq 2$ while maintaining accuracy.

The Doppler estimator also reaches its knee point at $n = 10$, where the runtime similarly starts to asymptotically approach the odometry runtime, although this computational bottleneck is only around 10 ms per frame for Doppler odometry. However, since the Doppler estimator is more susceptible to drift, there is a steeper decline in accuracy beyond the knee point. The accuracy is particularly limited in orientation, as shown by its higher rotational RMSE compared to the ICP-based estimator. This limitation may be mitigated by incorporating a higher-accuracy gyroscope.

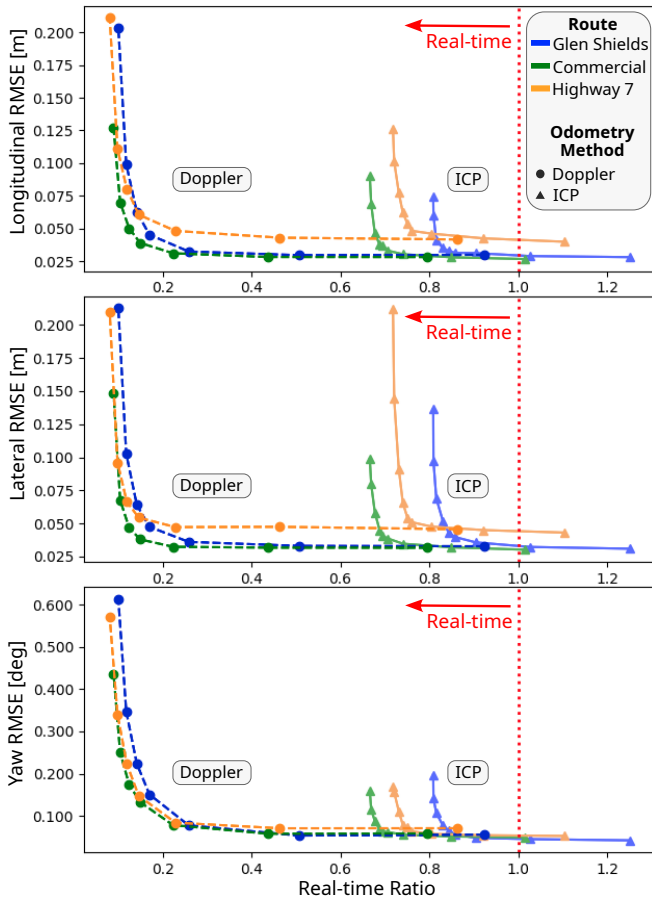


Fig. 3. Pareto front plots for the longitudinal (top), lateral (middle), and yaw (bottom) RMSE, comparing Doppler and ICP-based odometry methods across three routes. The plots show the trade-off between error and computational effort, with markers representing each tested interval. For the Doppler pipeline, the intervals are $n = 1, 2, 5, 10, 15, 25, 50$, while for the ICP pipeline, the intervals are $n = 1, 2, 5, 10, 15, 25, 50, 100, 150$.

When using $n \geq 50$ for the Doppler estimator and $n \geq 150$ for the ICP estimator, accumulated odometric drift leads to localization failure. Beyond these points, the RMSE in each translational component exceeds 0.2 m, making the estimate unusable in real-world applications.

3) *Trajectory Performance*: The Glen Shields and Commercial routes have abundant static geometric features, making them more favourable for both estimation methods. The ICP-based estimator has more stable correspondences for pointcloud alignment, while the Doppler estimator has better inlier classification. The Highway 7 route presents a greater challenge due to sparser geometric features, resulting in fewer points and a larger number of dynamic outliers. As the localization interval increases, both pipelines struggle to localize using the limited information available for alignment, resulting in error accumulating more rapidly.

The runtime comparison in Fig. 3 reveals that the Doppler-based estimator maintains consistent performance across the routes, while the ICP-based estimator’s runtime varies more significantly. This is because the Doppler estimator does not rely on scene geometry and efficiently solves a linear

system at each frame, resulting in a repeatable computational cost. In contrast, the ICP-based estimator iteratively aligns pointclouds, and its runtime depends on the number and quality of features available in the scene.

4) *Recommendations and Extensions*: This work demonstrates that our choice of odometry method can significantly reduce computational overhead in localization systems. The introduction of the lightweight Doppler method in a localization pipeline shows that fast estimations can be used when real-time performance is critical, leaving computational resources available for tasks other than localization. Although the Doppler odometry method performs worse in odometry evaluations [6], we demonstrate here that it can still be effectively used in a localization pipeline for significant computational savings with a negligible sacrifice in accuracy when localizing using small intervals. This highlights an important insight: odometry methods do not need to be highly accurate to contribute to highly accurate localization.

By controlling the frequency of localization attempts, rather than attempting to localize at each available instance, we show how localization efficiency can be improved without sacrificing accuracy. Using higher-accuracy odometry methods allows for larger intervals between localization updates, demonstrating that accuracy trade-offs can be achieved without altering the fundamental algorithms. This approach highlights the potential for customizing localization performance based on the operational objectives.

Future work can explore the use of dynamic intervals, where the localization frequency is adjusted in real-time based on system performance metrics. For example, a system could select the interval based on the current vehicle speed, route complexity, available computational resources, or estimator uncertainty. This would further optimize the localization process, making it more adaptable to varying conditions and constraints.

V. CONCLUSION

This paper studies improving the efficiency of lidar-based localization. We demonstrate that using a fast Doppler odometry method in a localization pipeline can significantly reduce computational overhead without sacrificing accuracy. Additionally, relying on odometry for extended periods between localization updates can balance the trade-off between computational effort and localization performance. For example, using a performance-oriented ICP-based odometry algorithm and localizing every 10 frames reduces the overall ICP pipeline runtime by 30%, while maintaining an accuracy below 0.05 m in translation and 0.1° in rotation. In contrast, when using a lightweight and less accurate Doppler odometry algorithm, the frequency of localization updates cannot be reduced as much, but the overall runtime is significantly lower. In this case, localizing every 10 frames results in an 80% reduction in runtime, with an accuracy below 0.06 m in translation and 0.18° in rotation. Overall, our results show that we can improve computational efficiency and maintain accuracy in existing localization pipelines, leaving resources available for other tasks within the AV pipeline.

REFERENCES

- [1] K. Burnett, Y. Wu, D. J. Yoon, A. P. Schoellig, and T. D. Barfoot, "Are We Ready for Radar to Replace Lidar in All-Weather Mapping and Localization?" *IEEE Robotics and Automation Letters*, vol. 7, no. 4, pp. 10 328–10 335, 2022.
- [2] D. Kumar and N. Muhammad, "A Survey on Localization for Autonomous Vehicles," *IEEE Access*, vol. 11, pp. 115 865–115 883, 2023.
- [3] P. J. Besl and N. D. McKay, "A Method for Registration of 3-D Shapes," *IEEE Trans. Pattern Anal. Mach. Intell.*, vol. 14, pp. 239–256, 1992.
- [4] F. Pomerleau, F. Colas, and R. Y. Siegwart, "A Review of Point Cloud Registration Algorithms for Mobile Robotics," *Found. Trends Robotics*, vol. 4, pp. 1–104, 2015.
- [5] Y. Wu, D. J. Yoon, K. Burnett, *et al.*, "Picking up Speed: Continuous-Time Lidar-Only Odometry Using Doppler Velocity Measurements," *IEEE Robotics and Automation Letters*, vol. 8, pp. 264–271, 2022.
- [6] D. J. Yoon, K. Burnett, J. Laconte, *et al.*, "Need for Speed: Fast Correspondence-Free Lidar-Inertial Odometry Using Doppler Velocity," in *2023 IEEE/RSJ International Conference on Intelligent Robots and Systems (IROS)*, 2023, pp. 5304–5310.
- [7] I. Vizzo, T. Guadagnino, B. Mersch, L. Wiesmann, J. Behley, and C. Stachniss, "KISS-ICP: In Defense of Point-to-Point ICP – Simple, Accurate, and Robust Registration If Done the Right Way," *IEEE Robotics and Automation Letters*, vol. 8, no. 2, pp. 1029–1036, 2023.
- [8] P. Dellenbach, J.-E. Deschaud, B. Jacquet, and F. Goulette, "CT-ICP: Real-time Elastic LiDAR Odometry with Loop Closure," in *2022 International Conference on Robotics and Automation (ICRA)*, 2022, pp. 5580–5586.
- [9] K. Chen, R. Nemiroff, and B. T. Lopez, "Direct LiDAR-Inertial Odometry: Lightweight LIO with Continuous-Time Motion Correction," in *2023 IEEE International Conference on Robotics and Automation (ICRA)*, 2023, pp. 3983–3989.
- [10] H. Ye, Y. Chen, and M. Liu, "Tightly Coupled 3D Lidar Inertial Odometry and Mapping," in *2019 International Conference on Robotics and Automation (ICRA)*, 2019, pp. 3144–3150.
- [11] S. Zhao, H. Zhang, P. Wang, L. Nogueira, and S. A. Scherer, "Super Odometry: IMU-centric LiDAR-Visual-Inertial Estimator for Challenging Environments," *2021 IEEE/RSJ International Conference on Intelligent Robots and Systems (IROS)*, pp. 8729–8736, 2021.
- [12] T. Shan, B. Englot, D. Meyers, W. Wang, C. Ratti, and D. Rus, "LIO-SAM: Tightly-coupled Lidar Inertial Odometry via Smoothing and Mapping," *2020 IEEE/RSJ International Conference on Intelligent Robots and Systems (IROS)*, pp. 5135–5142, 2020.
- [13] J. Zhang and S. Singh, "Low-drift and Real-time Lidar Odometry and Mapping," *Autonomous Robots*, vol. 41, no. 2, pp. 401–416, 2017.
- [14] K. Burnett, A. P. Schoellig, and T. D. Barfoot, "Continuous-Time Radar-Inertial and Lidar-Inertial Odometry Using a Gaussian Process Motion Prior," *IEEE Transactions on Robotics*, vol. 41, pp. 1059–1076, 2025.
- [15] K. Yoneda, H. Tehrani, T. Ogawa, N. Hukuyama, and S. Mita, "Lidar Scan Feature for Localization with Highly Precise 3-D Map," in *2014 IEEE Intelligent Vehicles Symposium Proceedings*, 2014, pp. 1345–1350.
- [16] H. Badino, D. Huber, and T. Kanade, "Visual Topometric Localization," in *2011 IEEE Intelligent Vehicles Symposium (IV)*, 2011, pp. 794–799.
- [17] P. Furgale and T. Barfoot, "Visual Teach and Repeat for Long-Range Rover Autonomy," *J. Field Robotics*, vol. 27, pp. 534–560, Sep. 2010.
- [18] D. Landry and P. Giguère, "Automating Node Pruning for LiDAR-Based Topometric Maps in the Context of Teach-and-Repeat," in *2016 13th Conference on Computer and Robot Vision (CRV)*, 2016, pp. 132–139.
- [19] J. Niedzwiedzki, A. Niewola, P. Lipinski, *et al.*, "Real-Time Parallel-Serial LiDAR-Based Localization Algorithm with Centimeter Accuracy for GPS-Denied Environments," *Sensors*, vol. 20, no. 24, p. 7123, 2020.
- [20] T. Shan and B. Englot, "LeGo-LOAM: Lightweight and Ground-Optimized Lidar Odometry and Mapping on Variable Terrain," in *2018 IEEE/RSJ International Conference on Intelligent Robots and Systems (IROS)*, 2018, pp. 4758–4765.
- [21] M. Zhao, J. Wang, T. Gao, C. Xu, and H. Kong, "FMCW-LIO: A Doppler LiDAR-Inertial Odometry," *IEEE Robotics and Automation Letters*, vol. 9, no. 6, pp. 5727–5734, 2024.
- [22] C. Pang, Z. Shen, R. Wu, and Z. Fang, "Efficient Doppler LiDAR Odometry Using Scan Slicing and Vehicle Kinematics," *IEEE Transactions on Instrumentation and Measurement*, vol. 74, pp. 1–13, 2025.
- [23] B. Behroozpour, P. A. M. Sandborn, M. C. Wu, and B. E. Boser, "Lidar System Architectures and Circuits," *IEEE Communications Magazine*, vol. 55, pp. 135–142, 2017.
- [24] B. Hexsel, H. Vhavle, and Y. Chen, "DICP: Doppler Iterative Closest Point Algorithm," in *Proceedings of Robotics: Science and Systems*, New York City, NY, USA, 2022.
- [25] D. Vivet, P. Checchin, and R. Chapuis, "Localization and Mapping Using Only a Rotating FMCW Radar Sensor," *Sensors (Basel, Switzerland)*, vol. 13, pp. 4527–4552, 2013.
- [26] D. Kellner, M. Barjenbruch, J. Klappstein, J. Dickmann, and K. Dietmayer, "Instantaneous Ego-Motion Estimation using Doppler Radar," in *16th International IEEE Conference on Intelligent Transportation Systems (ITSC 2013)*, 2013, pp. 869–874.
- [27] A. Kramer, C. Stahoviak, A. Santamaria-Navarro, A.-a. Aghamohammadi, and C. Heckman, "Radar-Inertial Ego-Velocity Estimation for Visually Degraded Environments," in *2020 IEEE International Conference on Robotics and Automation (ICRA)*, 2020, pp. 5739–5746.
- [28] Y. S. Park, Y.-S. Shin, J. Kim, and A. Kim, "3D Ego-Motion Estimation Using low-Cost mmWave Radars via Radar Velocity Factor for Pose-Graph SLAM," *IEEE Robotics and Automation Letters*, vol. 6, no. 4, pp. 7691–7698, 2021.
- [29] V. Kubelka, E. Fritz, and M. Magnusson, "Do We Need Scan-Matching in Radar Odometry?" in *2024 IEEE International Conference on Robotics and Automation (ICRA)*, 2024, pp. 13 710–13 716.
- [30] P. Gao, S. Zhang, W. Wang, and C. X. Lu, "DC-Loc: Accurate Automotive Radar Based Metric Localization with Explicit Doppler Compensation," in *2022 International Conference on Robotics and Automation (ICRA)*, 2022, pp. 4128–4134.
- [31] D. Lissus, K. Burnett, D. J. Yoon, R. Poulton, J. Marshall, and T. D. Barfoot, "Are Doppler Velocity Measurements Useful for Spinning Radar Odometry?" *IEEE Robotics and Automation Letters*, vol. 10, no. 1, pp. 224–231, 2025.
- [32] M. Paton, K. MacTavish, M. Warren, and T. D. Barfoot, "Bridging the Appearance Gap: Multi-Experience Localization for Long-Term Visual Teach and Repeat," in *2016 IEEE/RSJ International Conference on Intelligent Robots and Systems (IROS)*, 2016, pp. 1918–1925.
- [33] M. Paton, K. MacTavish, L.-P. Berczi, S. K. van Es, and T. D. Barfoot, "I Can See for Miles and Miles: An Extended Field Test of Visual Teach and Repeat 2.0," in *International Symposium on Field and Service Robotics*, 2017.
- [34] M. A. Fischler and R. C. Bolles, "Random Sample Consensus: A Paradigm for Model Fitting with Applications to Image Analysis and Automated Cartography," *Commun. ACM*, vol. 24, no. 6, pp. 381–395, Jun. 1981.
- [35] D. Kellner, M. Barjenbruch, J. Klappstein, J. Dickmann, and K. Dietmayer, "Instantaneous Ego-Motion Estimation using Multiple Doppler Radars," in *2014 IEEE International Conference on Robotics and Automation (ICRA)*, 2014, pp. 1592–1597.
- [36] T. D. Barfoot, C. H. Tong, and S. Särkkä, "Batch Continuous-Time Trajectory Estimation as Exactly Sparse Gaussian Process Regression.," in *Robotics: Science and Systems*, Citeseer, vol. 10, 2014, pp. 1–10.
- [37] S. Anderson and T. D. Barfoot, "Full STEAM Ahead: Exactly Sparse Gaussian Process Regression for Batch Continuous-Time Trajectory Estimation on SE(3)," in *2015 IEEE/RSJ International Conference on Intelligent Robots and Systems (IROS)*, 2015, pp. 157–164.
- [38] T. D. Barfoot, *State Estimation for Robotics*. Cambridge University Press, 2023.
- [39] K. Burnett, D. J. Yoon, Y. Wu, *et al.*, "Boreas: A Multi-Season Autonomous Driving Dataset," *The International Journal of Robotics Research*, vol. 42, no. 1–2, pp. 33–42, 2023.